In-situ self-templating construction of FeNi/N co-doped 3D porous carbon from bimetallic ions-coordinated porous organic polymer for rechargeable zinc-air batteries

Qi Xiong [a], Jiahui Zheng [a], Bei Liu [a], Yijiang Liu [a], Huaming Li [a,b,*], Mei Yang [a,b,*]

[a] College of Chemistry, Xiangtan University, Xiangtan 411105, Hunan Province, PR China
[b] Key Laboratory of Polymeric Materials & Application Technology of Hunan Province, Key Laboratory of Advanced Functional Polymeric Materials of College of Hunan Province, and Key Lab of Environment-Friendly Chemistry and Application in Ministry of Education, Xiangtan University, Xiangtan 411105, Hunan Province, PR China

ARTICLE INFO

ABSTRACT

Herein, an in-situ self-templating approach is applied to construct FeNi/N co-doped 3D porous carbon from bimetallic (Fe/Ni) ions-coordinated porous organic polymer (denoted as OPOP-FeNi). The OPOP-FeNi precursor is synthesized by polycondensation of sodium benzene-1,3,5-tris(olate) with cyanuric chloride followed by co-ordination with Fe^{3+}/Ni^{2+}, in which the in-situ generated NaCl can serve as template for the construction of 3D-interconnected hierarchical porous architecture during the pyrolysis process. The as-constructed FeNi/N-C-800 can offer high electrocatalytic activities toward ORR/OER with a high half-wave potential of 0.845 V (vs. RHE) in ORR and a low potential of 1.600 V (vs. RHE) at 10 mA cm^{-2} in OER. The outstanding ORR/OER activities render FeNi/N-C-800-based rechargeable zinc-air battery (RZAB) with long cycling life (1500 cycles/1000 h at 5.0 mA cm^{-2}), much more stable than previous reports on RZABs. Moreover, DFT calculations and poisoning experiments have been conducted to unveil the outstanding bifunctional activity of FeNi/N-C-800 electrocatalyst.

1. Introduction

Rechargeable zinc-air batteries (RZABs) have recently been recognized as one of the most promising energy storage devices owing to their peculiar merits such as high theoretical energy density, trustworthy safety, low-cost and eco-friendliness [1–4]. However, the practically attainable energy densities of RZABs reach only 40–50 % of their theoretical levels even if their theoretical energy densities can be as high as 1350 Wh kg^{-1}. The big gap between their theoretical and attainable energy densities is undoubtedly attributed to the kinetically sluggish oxygen reduction/evolution reaction (ORR/OER) that respectively occurred at the air electrode during the discharging and the charging process [5–7]. In order to improve the attainable energy densities of RZABs, it necessitates highly efficient, bifunctional oxygen electrocatalysts that can simultaneously accelerate ORR and OER. It is important to note that although Pt-based electrocatalysts can offer extremely high ORR activity and Ru- and Ir-based electrocatalysts can deliver outstanding OER activity, none are capable of catalyzing the ORR and OER simultaneously. In addition, the scarcity, high-cost, and poor

stability of such noble metal-based electrocatalysts hindered their practical applications in RZABs [8–10]. Therefore, rational design and construction of high-efficient and cost-effective bifunctional oxygen electrocatalysts are highly necessitated.

Transition-bimetal- and N-codoped porous carbons (denoted as $M_1M_2/N - C$, M_1M_2 = FeNi, FeCo, NiCo, etc.), deemed recently as a promising class of bifunctional oxygen electrocatalysts, have attracted increasing attention [11–18]. The outstanding bifunctional ORR/OER activities of $M_1M_2/N - C$ electrocatalysts have been found to be correlated with the in-situ formed N-doping configurations (i.e., graphitic-N and pyridinic-N), $M-N_x$ (i.e., M_1-N_x and M_2-N_x) species, and M_1M_2 alloy nanoparticles, in which N-doping configurations and $M-N_x$ species account for the high ORR activity, whereas alloyed M_1M_2 nanoparticles and $M-N_x$ species are responsible for the outstanding OER activity [19–21]. Among these $M_1M_2/N - C$ electrocatalysts, the high ORR/OER bifunctional activities of FeNi/N − C electrocatalysts have been experimentally and theoretically demonstrated. The introduction of alloyed FeNi nanoparticles into N-doped carbon can induce charge redistribution on the formed Fe–Ni atomic bonds, adjust the electronic structure of

---

neighboring Fe–Ni dual metal sites, which are the active sites for both OER and ORR [22]. In addition, the synergistic effect of Fe–Ni atomic pairs and N-doped carbon can optimize the binding energies of oxygen intermediates at Fe–Ni dual sites and decrease the energy barriers for all of the ORR/OER elementary steps, further promoting the bifunctional ORR/OER activities. Currently, the most common synthetic route to FeNi/N − C electrocatalysts is directly pyrolyzing bimetallic ions (Fe^{3+}/Ni^{2+})-coordinated porous organic polymers [23,24]. However, the direct pyrolysis of bimetallic ions-containing organic polymer precursors with soft networks at high temperature often suffers from the collapse of carbon skeletons, leading to a decrease in the specific surface areas (SSA) as well as the exposed active sites [25–28]. Moreover, the collapse of carbon skeletons during pyrolysis would undoubtedly cause the aggregation of metal nanoparticles. To address these issues, porous organic polymer precursors with robust networks and/or templating methods have been applied to enhance porosity and prevent metal nanoparticle agglomeration [29–38]. By comparison, hydrosoluble inorganic salt (i.e., NaCl, KCl, etc.) templates offer several advantages such as low-toxicity, low-cost and easy removal [35–38]. In addition, the use of hydrosoluble salt template can generate 3D-interconnected hierarchical porous architectures during the pyrolysis process and can help to avoid the excessive loss of heteroatoms.

Herein, an in-situ self-templating strategy is proposed to fabricate FeNi/N co-doped 3D porous carbon from bimetallic ions (Fe^{3+}/Ni^{2+})-coordinated porous organic polymer (denoted as OPOP-FeNi) precursor that was synthesized by polycondensation of cyanuric chloride with sodium benzene-1,3,5-tris(olate) followed by coordination with bimetallic ions (Fe^{3+}/Ni^{2+}). The in-situ generated NaCl salt can serve as template for the construction of 3D-interconnected hierarchical pore architecture during the pyrolysis process. With the assistance of NaCl template, a 3D-interconnected hierarchical porous N-doped carbon with FeNi alloy nanoparticles encapsulation (denoted as FeNi/N-C-800) is constructed under the optimized pyrolysis conditions. The OPOP network consisting of covalently linked triazinyl and benzene-1,3,5-trisoxyl units together with pore-filled NaCl can endow it with high skeleton strength together with high N/O contents, which facilitate not only metal ions coordination, but also high-level N/O co-doping and 3D-interconnected hierarchical pore architecture formation upon pyrolysis. As a result, the as-constructed FeNi/N-C-800 bifunctional electrocatalyst possessed a 3D-interconnected hierarchical pore structure together with high level of N-doping and alloyed FeNi nanoparticles encapsulation, which manifested outstanding bifunctional ORR/OER activity and utility in long-life RZABs.

2. Experimental section

2.1. Preparation of FeNi/N-C catalyst

Typically, 1,3,5-trihydroxybenzene (1.290 g, 10.00 mmol) and NaOH (1.250 g, 30.00 mmol) were dissolved in deionized water (120.0 mL) at 25 °C. After cooling to 0 °C, a solution of cyanuric chloride (1.860 g, 10.00 mmol) in ethanol (120.0 mL) was added dropwise followed by stirring at this temperature for 2 h. The reaction mixture was heated at reflux for another 24 h, then cooled down to ambient temperature. $Fe(NO_3)_3$ (1.210 g, 3.00 mmol) and $Ni(NO_3)_2$ (0.870 g, 3.00 mmol) were added and stirred for 0.5 h. The OPOP-FeNi precursor was obtained after vacuum freeze drying. For the preparation of FeNi/N-C-*x* electrocatalysts (*x* represents pyrolysis temperature), OPOP-FeNi precursor together with the in-situ generated NaCl were directly pyrolyzed under Ar atmosphere for 2 h at 700, 800, and 900 °C, respectively, and finally, the used NaCl template was removed by thoroughly washing with hot water. A similar procedure was used to synthesize Fe/N-C-800 and Ni/N-C-800 electrocatalysts at the optimal temperature (800 °C), except that the metal salts were separately replaced by $Fe(NO_3)_3$ (2.420 g, 6.00 mmol) and $Ni(NO_3)_2$ (1.740 g, 6.00 mmol), respectively. For comparison, OPOP without NaCl was also pyrolyzed under Ar

atmosphere for 2 h at 800 °C and the product was labeled as N-C-800.

2.2. Electrochemical measurements

The ORR and OER measurements were performed in the typical three-electrode system by using the Gamry-1010E electrochemical workstation at 25 °C. Glassy carbon rotating disk electrode (5.0 mm in diameter) or rotating ring disc electrode (5.6 mm in diameter), graphite rod and Hg/HgO were used as working electrode, counter electrode and reference electrode, respectively. The mass-loading of electrocatalysts on the glassy carbon disk electrode was 0.40 mg cm^{-2}. All experiments were performed in N_2- or O_2-saturated 0.1 M KOH solutions. Further details of associated tests and related calculations were described in Supporting Information.

2.3. Zn-air battery tests

The battery performance was evaluated on a home-made electrochemical cell at atmospheric conditions. 6.0 M KOH solution comprised 0.2 M zinc acetate was served as the electrolyte. For the assembly of RZABs, the treated Zn plate, carbon paper coated with electrocatalyst (electrocatalyst loading = 1.50 mg cm^{-2}), and 6.0 M KOH/0.2 M Zn (OAc)$_2$ solution were used as anode, air cathode, and electrolyte, respectively. For comparison, Pt/C||IrO$_2$-based RZAB (the mass ratio of Pt/C: IrO$_2$ = 1:1) was also assembled. Further details of associated tests and related calculations were described in Supporting Information.

3. Results and discussion

3.1. Preparation and characterization of FeNi/N-C-x electrocatalysts

A detailed schematic depiction of the preparation of FeNi/N-C-*x* electrocatalysts was displayed in Fig. 1. In a typical fabrication process, sodium benzene-1,3,5-tris(olate) was firstly synthesized through neutralization reaction between 1,3,5-trihydroxybenzene and NaOH in aqueous solution. The oxygen-bridged porous organic polymer (denoted as OPOP) was then synthesized via nucleophilic substitution of halogen in cyanuric chloride with sodium benzene-1,3,5-tris(olate). The OPOP-FeNi precursor was finally fabricated by coordination of OPOP with Fe^{3+}/Ni^{2+} cations. The successful formation of OPOP network was verified by FT-IR, TGA, and N_2 sorption analyses (Figure S2-S4). The SSA and total pore volume (V_t) of pure OPOP was found to be 41 m^2 g^{-1} and 0.20 cm^3 g^{-1} (Figure S4), much higher than that of NaCl-encapsulated OPOP (denoted as OPOP/NaCl). In contrast, OPOP/NaCl possessed significantly higher thermostability than that of pure OPOP (Figure S3), as evidenced by TGA analysis, highlighting the importance of NaCl template. The pore-filled NaCl in OPOP network can effectively prevent the collapse of carbon skeletons during pyrolysis. In addition, the coordination of Fe^{3+}/Ni^{2+} cations in OPOP network was also confirmed by FT-IR analysis (Figure S2). With the assistance of NaCl template, the FeNi/N-C-*x* electrocatalysts were fabricated by directly pyrolyzing NaCl-encapsulated OPOP-FeNi precursor (denoted as OPOP-FeNi/NaCl) at different temperatures (Fig. 1). Electrochemical tests demonstrated that the optimal molar ratio of OPOP/Fe(NO$_3$)$_3$/Ni(NO$_3$)$_2$ was 1/0.3/0.3 (Figure S5), we therefore adopted this synthetic condition and then systemically studied the effect of pyrolysis temperature.

XRD analysis implied that FeNi alloy phase was successfully generated in the FeNi/N-C-800 electrocatalyst, as verified by the appearance of three characteristic peaks at 43.6°, 50.8° and 74.7° (Fig. 2a), which can be assigned to the (111), (200) and (220) planes of FeNi alloy (JCPDS, PDF 47–1405). As for the Ni/N-C-800 and Fe/N-C-800 electrocatalysts, only metallic Ni and Fe peaks were observed in their XRD patterns (Fig. 2a), i.e., peaks at 44.5°, 51.8° and 76.4° corresponding to the (111), (200) and (220) planes of metallic Ni (JCPDS, PDF 04–0850), peaks at 44.7° and 65.0° corresponding to the (110) and (200) planes of metallic Fe (JCPDS, PDF 06–0696). In addition, a trace amount of Fe$_3$C
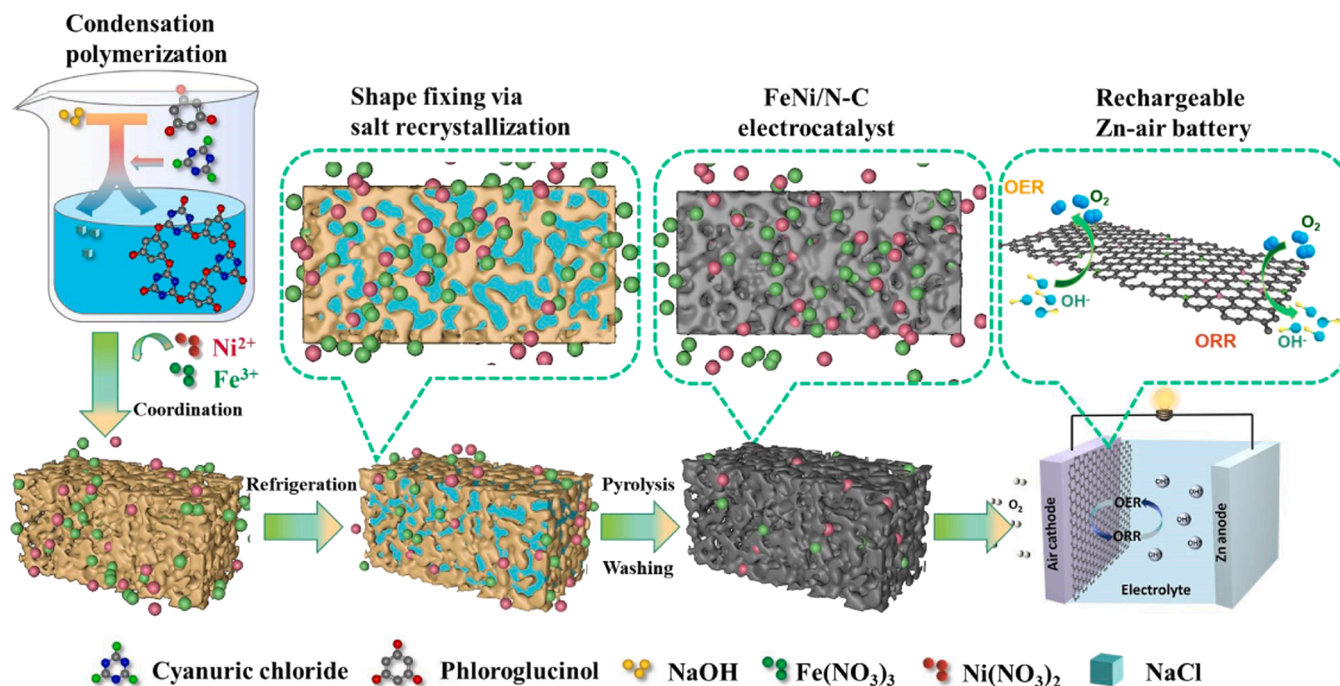
Fig. 1. Schematic depiction of the preparation of FeNi/N-C-*x* electrocatalysts.

was formed in the FeNi/N-C-800 electrocatalyst, which was probably due to the partially dissolution of C atoms into Fe lattice during the process of high-temperature pyrolysis [39,40]. To determine the Fe/Ni contents of FeNi/N-C-800 electrocatalyst, inductively coupled plasma atomic emission spectrometry (ICP-AES) measurement was performed. The Fe/Ni contents in FeNi/N-C-800 electrocatalyst were found to be 6.54 wt. % Fe and 6.49 wt. % Ni (Table S1), which is consistent with the TGA analysis (Figure S6). More structural information for FeNi/N-C-*x* electrocatalysts was provided by Raman spectroscopy. As illustrated in Fig. 2b, the area ratio of D peak to G peak was estimated to be 2.26, 1.99 and 1.05, respectively, for the FeNi/N-C-700, FeNi/N-C-800 and FeNi/N-C-900 electrocatalysts (Table S2), suggesting relatively high graphitization of FeNi/N-C-900 electrocatalyst. Supporting evidence for this comes from the area ratios of sp^3 C to sp^2 C determined from their deconvoluted XPS C 1*s* spectra (Figure S7, Table S2) [7,41,42].

The morphology of FeNi/N-C-800 electrocatalyst was investigated by scanning electron microscope (SEM). As displayed in Figure S8, the FeNi/N-C-800 electrocatalyst possessed a 3D hierarchically porous architecture that consisted of aggregated, irregularly shaped nanoparticles. The transmission electron microscopy (TEM) verified that FeNi/N-C-800 electrocatalyst presented a 3D porous structure with metallic nanoparticles encapsulation (Fig. 2c-d). In the high-resolution TEM image of FeNi/N-C-800 electrocatalyst, lattice spacings for the (111) facet of FeNi alloy (~0.207 nm) and for the (002) face of graphitic carbon (~0.340 nm) could be clearly seen (Fig. 2e). The corresponding element mapping manifested the uniform distribution of C, N, O, Fe and Ni (Fig. 2f-j). Moreover, almost overlapped Fe and Ni signals again confirmed the formation of alloyed FeNi particles (Fig. 2k).

N₂ adsorption/desorption technique was introduced to evaluate the porosities of FeNi/N-C-*x* electrocatalysts. As shown in Fig. 3a-b, the N₂ isotherms of FeNi/N-C-*x* electrocatalysts exhibited characteristics of hierarchical pores (micropores, mesopores, and macropores), as evidenced by the rapid N₂ uptakes at both low and high P/P_0 as well as hysteresis loops at moderate P/P_0 [43,44]. Moreover, the pore size distribution profiles of FeNi/N-C-*x* electrocatalysts also confirmed the coexistence of mesopores and macropores (Fig. 3b and Table S3). The SSA and V_t of FeNi/N-C-800 electrocatalyst were found to be 219 m² g⁻¹ and 0.37 cm³ g⁻¹, higher than those of FeNi/N-C-700 electrocatalyst

(197 m² g⁻¹/0.30 cm³ g⁻¹) and FeNi/N-C-900 electrocatalyst (191 m² g⁻¹/0.36 cm³ g⁻¹). The interconnected 3D porous structure together with high porosity were expected to enhance the expose level of active species and promote mass and charge transfer in the ORR and OER.

X-ray photoelectron spectroscopy (XPS) technique was introduced to further analyze the surface composition and electronic state of FeNi/N-C-800 electrocatalyst. The survey XPS spectrum indicated the coexistence of C (284.8 eV, 84.22 at. %), N (398.9 eV, 7.16 at. %), O (531.7 eV, 5.63 at. %), Fe (711.3 eV, 1.50 at. %) and Ni (854.8 eV, 1.49 at. %) elements in the FeNi/N-C-800 electrocatalyst (Figure S9). In addition, the deconvoluted N 1*s* and O 1*s* XPS spectra demonstrated that N-doping configurations included pyridinic-N (398.7 eV, 60.59 %), metal-N$_x$ (399.7 eV, 9.44 %), pyrrolic-N (400.5 eV, 7.80 %), graphitic-N (401.2 eV, 18.69 %) and oxidized-N(402.7 eV, 4.33 %) (Fig. 3d), while O-doping configurations comprised of C=O (530.3 eV, 21.00 %), C-O (531.7 eV, 52.20 %), and C-OH (533.2 eV, 26.80 %) (Fig. 3c). Furthermore, high-resolution Fe 2*p* and Ni 2*p* XPS spectra confirmed the coexistence of high-valence state Fe (701 and 740 eV) and Ni (848 and 888 eV) as well as zero-valence state Fe (707.5 and 717.9 eV) and Ni (854.2 and 871.5 eV) (Fig. 3e, f) in FeNi/N-C-800 electrocatalyst. Undoubtedly, the high-valence state Fe and Ni in the FeNi/N-C-800 electrocatalyst should be associated with metal-N$_x$ species, i.e., Fe-N$_x$ [45] and Ni-N$_x$ [46] configurations, while the zero-valence state Fe and Ni were related to FeNi alloy [47,48]. Owing to the metal-N coordination, alloyed FeNi nanoparticles can be strongly coupled to the defect-rich N-doped porous carbon [12,42,45,49,50]. To prove this, XPS analysis was performed for Fe/N-C-800, Ni/N-C-800 and N-C-800 electrocatalysts. As displayed in Fig. 2c-d, the deconvoluted peaks of N 1*s* and O 1*s* spectra of FeNi/N-C-800 electrocatalyst were all shifted to higher binding energies, as compared to those of N-C-800 electrocatalyst, implying the strong electronic coupling between the FeNi alloy and the N-doped carbon [51]. Moreover, the contents of Fe-N$_x$ and Ni-N$_x$ configurations in the FeNi/N-C-800 electrocatalyst were significantly higher than those in the Fe/N-C-800 or the Ni/N-C-800 electrocatalysts (Fig. 2e-f), indicating the stronger interactions between the FeNi alloy and the N-doped carbon [52].
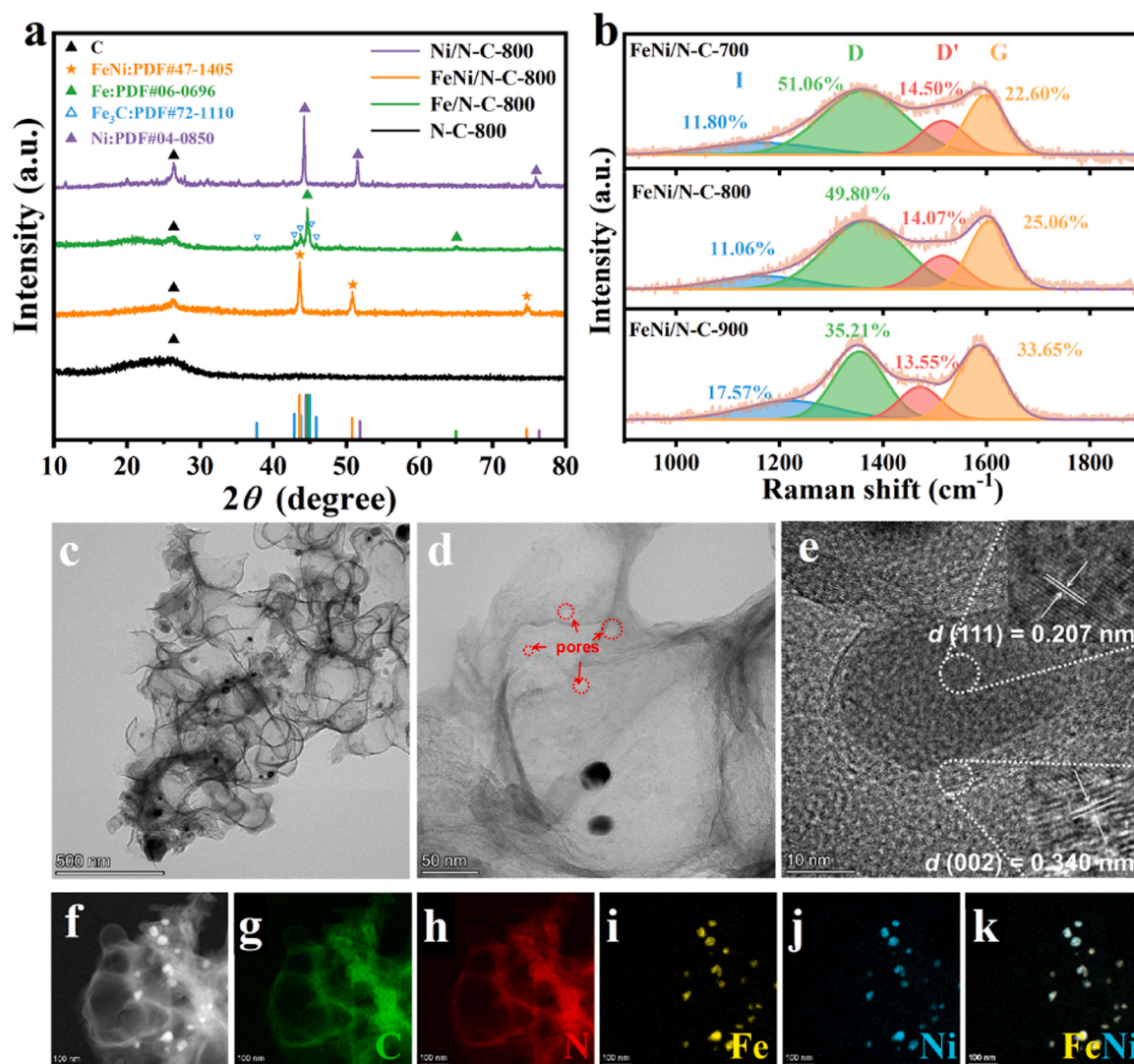
Fig. 2. XRD patterns of different catalysts (a). Raman spectra of FeNi/N-C-*x* (b). TEM and HR-TEM images (c-e), and elemental mapping images of FeNi/N-C-800 (f-k).

3.2. Bifunctional electrocatalytic activity of FeNi/N-C-x electrocatalysts

As mentioned above, the FeNi/N-C-800 electrocatalyst has hierarchically porous architecture, high SSA, high level of N-doping together with alloyed FeNi nanoparticles encapsulation, which render it applicable as a bifunctional oxygen electrocatalyst. Therefore, the ORR performance of FeNi/N-C-800 electrocatalyst was firstly evaluated in 0.1 M KOH solution. As displayed in Fig. 4a-b, FeNi/N-C-800 electrocatalyst presented a high electrocatalytic activity toward ORR with an onset potential (E_o) and half-wave potential ($E_{1/2}$) of 0.965 V (vs RHE) and 0.845 V (vs RHE), which are comparable to commercial Pt/C electrocatalyst but are significantly higher than those of Fe/N-C-800, Ni/N-C-800 and N-C-800 electrocatalysts. The outstanding ORR performance of FeNi/N-C-800 electrocatalyst was comparable or superior to those of non-noble metal-based electrocatalysts (Table S4). The Tafel slope was also examined to explore the ORR kinetic character on FeNi/N-C-800 electrocatalyst. As displayed in Fig. 4c, the Tafel slopes were found to be 77, 83, 119, 200, and 78 mV dec^{-1} for FeNi/N-C-800, Fe/N-C-800, Ni/N-C-800, N-C-800 and Pt/C electrocatalysts, respectively, suggesting the fast ORR kinetic on FeNi/N-C-800 electrocatalyst. The ORR pathway was explored by using RRDE tests. The calculated HO_2^- yield (%) was below 11.37 %, and the corresponding electron transfer number (*n*) was 3.68 – 3.86 for the FeNi/N-C-800 electrocatalyst (Fig. 4d), implying a

four-electron pathway toward ORR. The stability of FeNi/N-C-800 electrocatalyst was evaluated by the chronoamperometric measurements. As displayed in Fig. 4e, a slight current loss was observed for FeNi/N-C-800 electrocatalyst, demonstrating the excellent cycling stability.

Acid etching and SCN$^-$-poisoning experiments were performed to roughly determine the relative contribution of various ORR active sites by using $E_{1/2}$ value as the benchmark (see SI). Firstly, 9.0 M HNO$_3$ etching was performed on FeNi/N-C-800 electrocatalyst to completely eliminate FeNi alloy, M-N$_x$ and nitrogenated functionalities (i.e., pyridinic-N and graphitic-N in the current case, hereafter denoted as "N-c"), and the HNO$_3$-etched product was referred to as E-NC-800. As shown in Figure S13 and Fig. 4f, the $\Delta E_{1/2}$ value between E-NC-800 and N-C-800 electrocatalysts was about 220 mV, therefore the ORR contribution of N-c was about 64.71 % in the FeNi/N-C-800 electrocatalyst. Secondly, 1.0 M HCl etching was carried out on FeNi/N-C-800 electrocatalyst to remove FeNi alloy but retain M-N$_x$ species, the HCl-etched electrocatalyst was denoted as FeNi/N-C-800/HCl. Similarly, the ORR contribution of M-N$_x$ species was also evaluated by the $\Delta E_{1/2}$ value between FeNi/N-C-800/HCl and N-C-800 electrocatalysts, accounting for 26.47 % in the FeNi/N-C-800 electrocatalyst (Fig. 4f). Taken together, the relative contributions of N-c, M-N$_x$ species and bimetal alloy nanoparticles toward the ORR were found to be 64.71 %, 26.47 %,
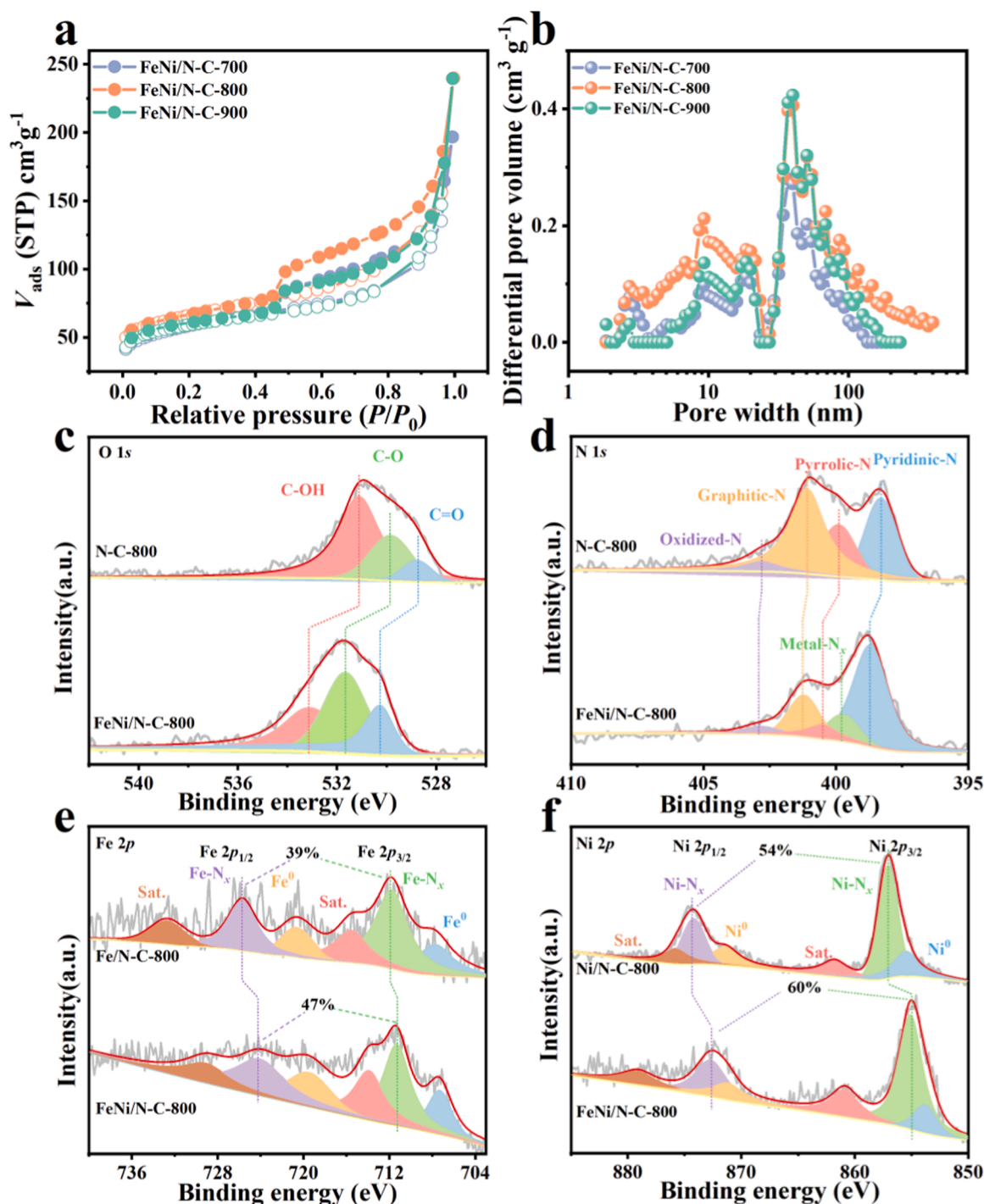
Fig. 3. N$_2$ adsorption-desorption isotherms (a) and corresponding pore size distribution (b) of FeNi/N-C-*x*. O 1*s* spectra (c), N 1*s* spectra (d) of FeNi/N-C-800 and N-C-800, Fe 2*p* spectra (e) of FeNi/N-C-800 and Fe/N-C-800, Ni 2*p* spectra (f) of FeNi/N-C-800 and Ni/N-C-800.

and 8.82 % in the FeNi/N-C-800 electrocatalyst.

In addition to the excellent ORR performance, FeNi/N-C-800 electrocatalyst also presented a highly electrocatalytic activity toward the OER. As presented in Fig. 5a, the FeNi/N-C-800 electrocatalyst manifested the most negative potential of 1.600 V (vs RHE) at 10 mA cm^{-2} ($E_{J=10}$) among the four electrocatalysts, and could compete with the IrO$_2$ electrocatalyst (1.600 V vs RHE) as well as other OER electrocatalysts reported recently (Table S4). These results indicate that the bimetal alloy nanoparticles are highly active toward OER [53–55]. The Tafel slope of FeNi/N-C-800 electrocatalyst was found to be 128 mV dec^{-1}, slightly higher than that of the IrO$_2$ electrocatalyst, indicating the

improved OER kinetics on FeNi/N-C-800 electrocatalyst (Fig. 5b). The long-term stability of FeNi/N-C-800 electrocatalyst was also studied by chronoamperometric measurements. Compared to the IrO$_2$ electrocatalyst, the FeNi/N-C-800 electrocatalyst exhibited superior stability, as evidenced by significantly higher current-retention (Fig. 5c). These results imply that the high degree of graphitization of FeNi/N-C-800 electrocatalyst can slow down the electrochemical corrosion and carbon oxidation [56,57]. In order to roughly estimate the OER contributions of various active sites in the FeNi/N-C-800 electrocatalyst, acid-etching and SCN$^-$-poisoning experiments was adopted again. As shown in Figure S15 and Fig. 5d, the OER contributions of bimetal alloy
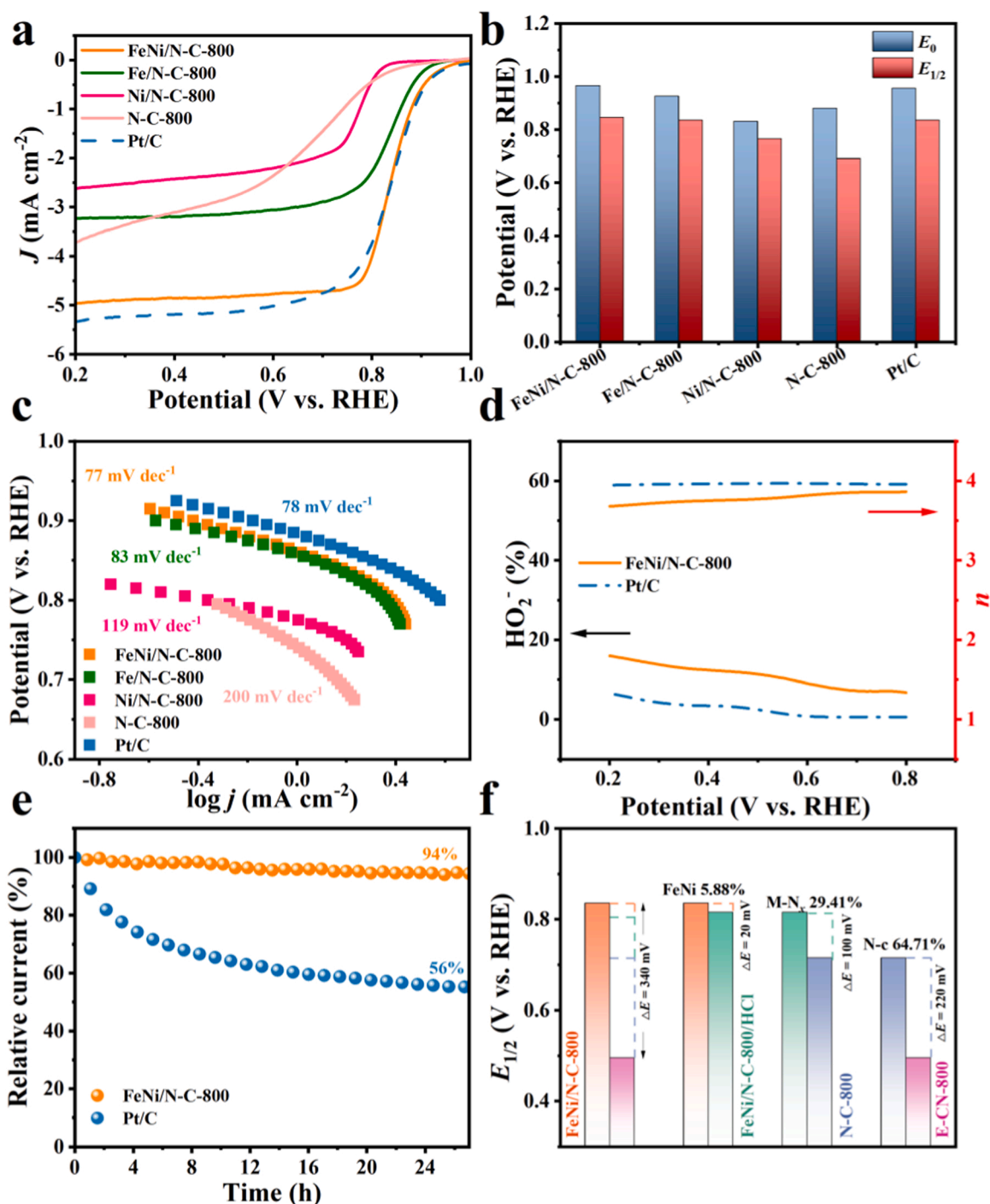
Fig. 4. ORR performance: OER polarization curves (a), the corresponding E_o and $E_{1/2}$ values (b) and Tafel plots (c)·H_2O^- yield and n (d), and i-t stability (e) for FeNi/N-C-800 and other control samples. The relative contribution of active species (f) in FeNi/N-C-800.

nanoparticles, M-N_x species, and nitrogenated functionalities were determined to be 45.37 %, 35.72 %, and 18.91 %, respectively, by using $E_{J=10}$ value as the benchmark. Undoubtedly, bimetal alloy nanoparticles, M-N_x species in the FeNi/N-C-800 electrocatalyst are mainly responsible for its outstanding OER performance. The reversible oxygen electrode activity in terms of potential gap between OER ($E_{J=10}$) and ORR ($E_{1/2}$) (ΔE, $\Delta E = E_{J=10} - E_{1/2}$) was found to be 0.755 V, which could compete with that of mixed Pt/C and IrO_2 electrocatalyst (Fig. 5e-f). The satisfactory bifunctional activity of FeNi/N-C-800 can be attributable to the abundant and uniformly distributed active sites together with the interconnected 3D hierarchical pore architecture and

high SSA, which can promote the exposure level of active sites and speed up the transport/diffusion of electrolyte ions.

3.3. Zn-air battery performance of FeNi/N-C-800 electrocatalyst

A homemade aqueous RZAB with FeNi/N-C-800 air cathode was assembled. The FeNi/N-C-800-based RZAB exhibited a stable open-circuit voltage (1.46 V), higher than that of Pt/C||IrO_2-based RZAB (1.42 V, Fig. 6a). The calculated specific capacity of FeNi/N-C-800-based RZAB reached up to 806 mAh g_{Zn}^{-1} at 5 mA cm^{-2} (Fig. 6b). In addition, the stable discharge voltage platforms at different current
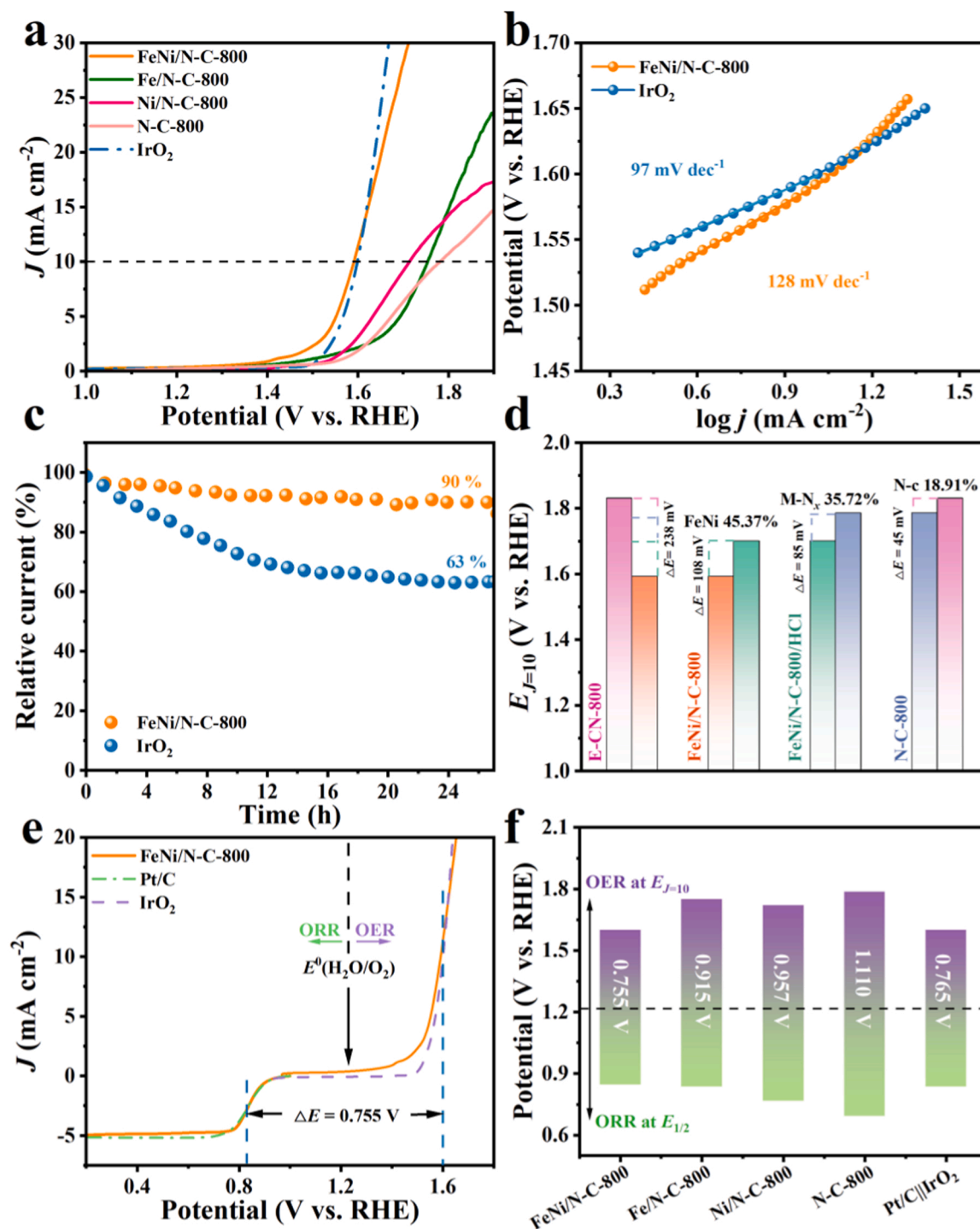
Fig. 5. OER performance: OER polarization curves (a), and corresponding Tafel plots (b), *i-t* stability (c), the relative contribution of active species (d), the overall polarization curves (e), the values of ΔE ($\Delta E = E_{j = 10} - E_{1/2}$) of FeNi/N-C-800 and other control samples (f).

densities indicated the excellent rate capacity of FeNi/N-C-800-based RZAB (Fig. 6c). The discharge polarization profiles and the corresponding power density of FeNi/N-C-800-based and Pt/C||IrO$_2$-based RZABs were presented in Fig. 6d. FeNi/N-C-800-based RZAB delivered a maximum power density of 115 mW cm^{-2}, corresponded closely to that of Pt/C||IrO$_2$-based RZAB (112 mW cm^{-2}). A yellow LED can be lighted by two FeNi/N-C-800-based RZABs connected in series (Fig. 6f). The rechargeability of FeNi/N-C-800-based RZAB was evaluated at 5 mA cm^{-2} and compared with Pt/C||IrO$_2$-based RZAB. As displayed in Fig. 6h, FeNi/N-C-800-based RZAB could be discharged and charged for

more than 1500 cycles/1000 h with a slight drop in energy efficiency (57 %), which surpassed that of Pt/C||IrO$_2$-based RZAB and other electrocatalysts-based RZABs reported recently (Fig. 6e, Table S4). After cycling test, the 3D-interconnected architecture of FeNi/N-C-800 electrocatalyst can be basically maintained (Fig. 6g). All of the above results confirmed the superb activity and cycling stability of our FeNi/N-C-800 electrocatalyst.

Density functional theory (DFT) calculations was undertaken to further explore the origin of the excellent ORR/OER activity. The Fe/N-C, Ni/N-C and FeNi/N-C were modeled, by a Fe$_4$ cluster, a Ni$_4$ cluster
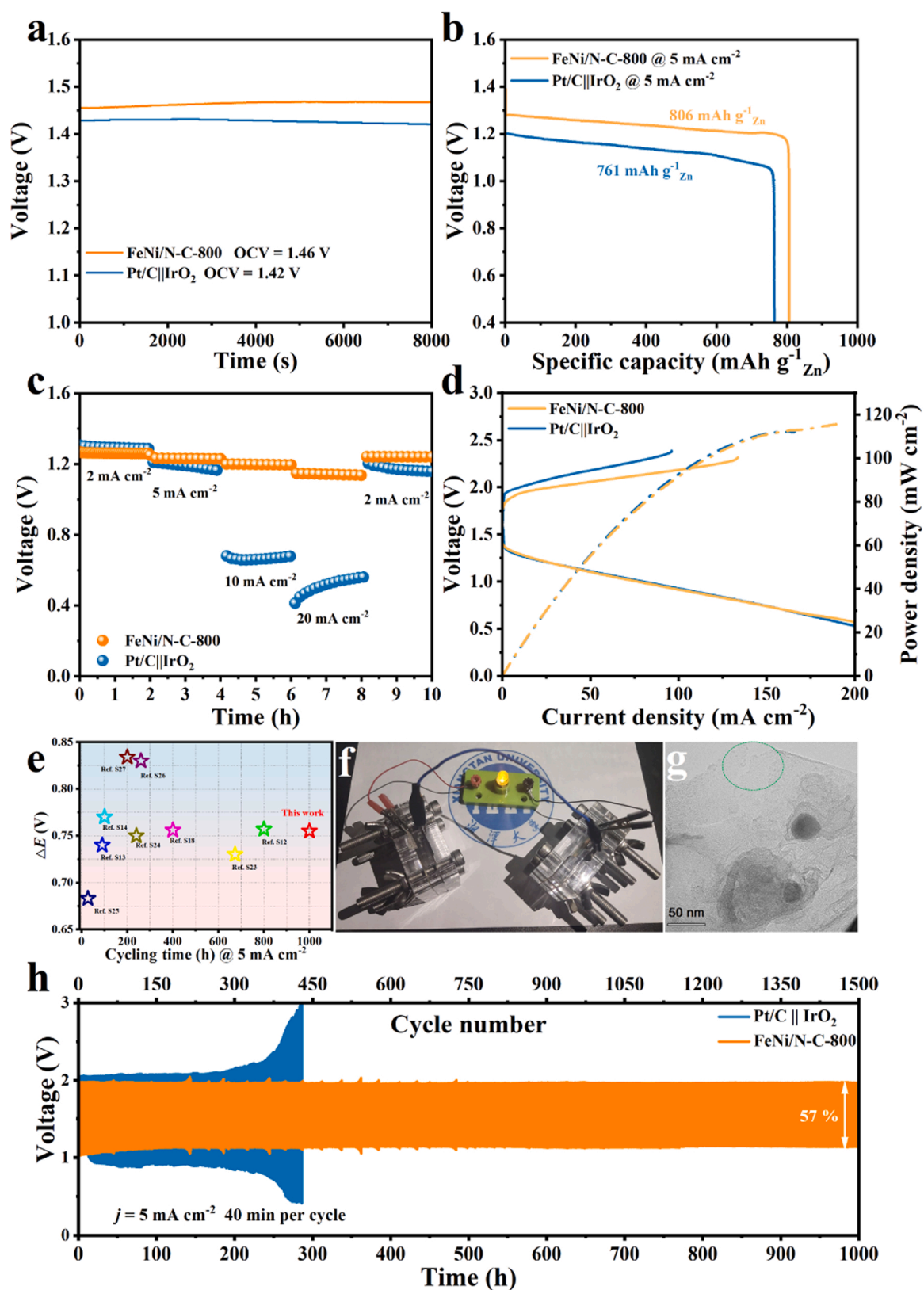
Fig. 6. RZABs pCCcapacities (b), rate discharge curves (c), discharge polarization and power density curves (d). A comparison with the reported RZABs in ΔE value and cycling durability (e). A lighted LED powered by two FeNi/N-C-800-based RZAB (f). TEM image of FeNi/N-C-800 after cycling (g). Cycling performance of FeNi/N-C-800-based and Pt/C||IrO₂-based RZABs (h).

and a Fe_2Ni_2 cluster encapsulated in N-doped carbon matrix [58–60], respectively (Fig. 7b-d). N-C with bare metal cluster was built as the control model (Fig. 7a). As displayed in Fig. 7e, compared to N-C model, the Fe/N-C, Ni/N-C and FeNi/N-C models all displayed metallic feature and their active C atoms achieved markedly improved electronic states below Fermi level. In addition, because more delocalized "electron-donating area" were introduced, the doping of N can help to enhance the adsorption of reaction intermediates onto the surface of carbon matrix [61]. These intrinsic qualities enabled the functionalized region on Fe/Ni decorated N-C with superior electrocatalytic activity.

Furthermore, the corresponding Gibbs free energy change (ΔG) were calculated on the Fe/N-C, Ni/N-C and FeNi/N-C models with an external potential (U) of 0 V. As presented in Fig. 7g-i, the downhill pathways toward ORR were exothermic reactions, which were regarded as follows: Step 1: $O_2 + *H + e^- \leftrightarrow *OOH$; Step 2: $*OOH + H^+ + e^- \leftrightarrow *O + H_2O$; Step 3: $*O + H^+ + e^- \leftrightarrow *OH$; and Step 4: $*OH + H^+ + e^- \leftrightarrow * H_2O$ (Fig. 7f) [51,62,63]. Among them, the elementary step with the smallest ΔGx ($x = 1, 2, 3, 4$) was the rate-limiting step (RLS). The limiting potential for ORR was defined as $U_{L(ORR)}$ [64], which was found to be 0.564 V, 0.627 V, and 0.857 V for Ni/N-C, Fe/N-C and FeNi/N-C, respectively, indicating the catalytic activity toward ORR increasing in the order of Ni/N-C < Fe/N-C < FeNi/N-C. For the OER, the inverse reaction of ORR,

the uphill steps were endergonic, and the elementary step with the largest ΔGx was the RLS. The limiting potential for OER was defined as $U_{L(OER)}$ [65], which was found to be 1.115 V, 0.719 V, and 0.477 V for Fe/N-C, Ni/N-C and FeNi/N-C, respectively. Apparently, FeNi/N-C also possessed the best OER performance (Fig. 7g-i). In general, the DFT calculations and the experimental results were in good agreement, highlighting the coupling of synergies between FeNi alloy and N-doped carbon matrix in generating advantageous surface electronic environment and therefore elevating the bifunctional activity toward ORR/OER.

4. Conclusion

In summary, a facile in-situ self-templating approach is applied to construct FeNi/N co-doped 3D porous carbon from bimetallic (Fe/Ni) ions-coordinated porous organic polymer (denoted as OPOP-FeNi). The OPOP-FeNi is synthesized by polycondensation of sodium benzene-1,3,5-tris(olate) with cyanuric chloride followed by coordination with Fe^{3+}/Ni^{2+}, in which the in-situ generated NaCl can serve as template for the construction of 3D-interconnected hierarchical porous architecture during the pyrolysis process. Benefiting from the 3D-interconnected hierarchical porous architecture together with the high level of N-
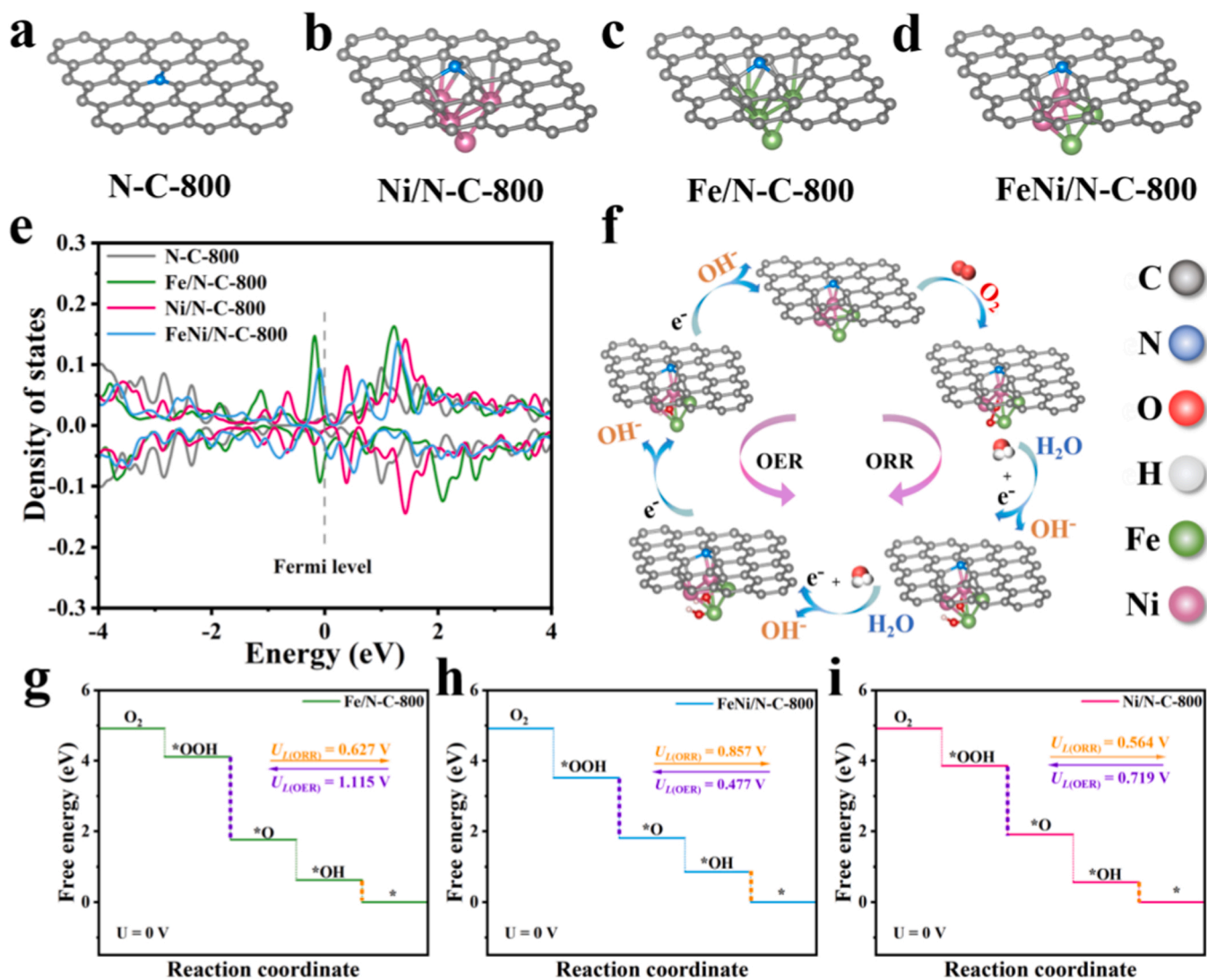

Fig. 7. Four DFT models: N-C (a), Ni/N-C (b), Fe/N-C (c) and FeNi/N-C (d). The projected density of states of the active C atoms in N-C, Ni/N-C, Fe/N-C and FeNi/N-C (e). The reaction pathways with the intermediates during the ORR/OER process on FeNi/N-C model (f). The free energy diagrams of OER and ORR on (g) Fe/N-C, (h) FeNi/N-C and (i) Ni/N-C at the U = 0 V. The orange and the purple dot lines are the RLS for ORR and OER, respectively.

doping (7.16 at. %) and alloyed FeNi nanoparticles incorporation, the optimized FeNi/N-C-800 electrocatalyst presents high bifunctional activity toward ORR/OER with a ΔE of 0.755 V. The outstanding ORR/OER activities render the FeNi/N-C-based ZAB with high rate performance and remarkable cycling stability (1500 cycles/1000 h at 5.0 mA cm^{-2}). The interplay between the alloyed FeNi nanoparticles and the 3D-interconnected hierarchical porous carbons and the abundant N-containing functional groups are demonstrated to be the essential factors to enhance the catalytic activity of FeNi/N-C-800. Our study provides a facile and effective strategy for constructing robust and cost-effective bifunctional oxygen electrocatalysts for high-performance energy conversion and storage systems.

CRediT authorship contribution statement

Qi Xiong: Methodology, Investigation, Data curation, Writing – original draft. **Jiahui Zheng:** Data curation. **Bei Liu:** Supervision. **Yijiang Liu:** Supervision. **Huaming Li** and **Mei Yang:** Supervision, Writing – review & editing.

Declaration of Competing Interest

The authors declare that they have no known competing financial interests or personal relationships that could have appeared to influence the work reported in this paper.

Data availability

l have shared the link to my data/code at the Attach File step.

Acknowledgments

Appendix A. Supporting information

Supplementary data associated with this article can be found in the online version at doi:10.1016/j.apcatb.2022.122067.

References

[1] Q. Zhou, L. Ai, Q. Li, S. Hou, L. Xu, D. Sun, H. Pang, K. Huang, Y. Tang, A. Ship-in-a-Bottle, strategy to anchor CoFe nanoparticles inside carbon nanowall-assembled frameworks for high-efficiency bifunctional oxygen electrocatalysis, Chem. Eng. J. 417 (2021), 127895, https://doi.org/10.1016/j.cej.2020.127895.

[2] X. Fu, G. Jiang, G. Wen, R. Gao, S. Li, M. Li, J. Zhu, Y. Zheng, Z. Li, Y. Hu, L. Yang, Z. Bai, A. Yu, Z. Chen, Densely accessible Fe-Nx active sites decorated mesoporous-carbon-spheres for oxygen reduction towards high performance aluminum-air flow batteries, Appl. Catal. B: Environ. 293 (2021), 120176, https://doi.org/10.1016/j.apcatb.2021.120176.

[3] C. Lai, J. Fang, X. Liu, M. Gong, T. Zhao, T. Shen, K. Wang, K. Jiang, D. Wang, In situ coupling of NiFe nanoparticles with N-doped carbon nanofibers for Zn-air batteries driven water splitting, Appl. Catal. B: Environ. 285 (2021), 119856, https://doi.org/10.1016/j.apcatb.2020.119856.

[4] M. Mazzucato, G. Daniel, A. Mehmood, T. Kosmala, G. Granozzi, A. Kucernak, C. Durante, Effects of the induced micro- and meso-porosity on the single site density and turn over frequency of Fe-N-C carbon electrodes for the oxygen reduction reaction, Appl. Catal. B: Environ. 291 (2021), 120068, https://doi.org/10.1016/j.apcatb.2021.120068.

[5] Z. Lu, B. Wang, Y. Hu, W. Liu, Y. Zhao, R. Yang, Z. Li, J. Luo, B. Chi, Z. Jiang, M. Li, S. Mu, S. Liao, J. Zhang, X. Sun, An isolated zinc–cobalt atomic pair for highly active and durable oxygen reduction, Angew. Chem. Int. Ed. 58 (2019) 2622–2626, https://doi.org/10.1002/anie.201810175.

[6] S. Ren, X. Duan, S. Liang, M. Zhang, H. Zheng, Bifunctional electrocatalysts for Zn–air batteries: recent developments and future perspectives, J. Mater. Chem. A 8 (2020) 6144–6182, https://doi.org/10.1039/C9TA14231B.

[7] A. Wang, C. Zhao, M. Yu, W. Wang, Trifunctional Co nanoparticle confined in defect-rich nitrogen-doped graphene for rechargeable Zn-air battery with a long lifetime, Appl. Catal. B: Environ. 281 (2021), 119514, https://doi.org/10.1016/j.apcatb.2020.119514.

[8] K. Gong, F. Du, Z. Xia, M. Durstock, L. Dai, Nitrogen-doped carbon nanotube arrays with high electrocatalytic activity for oxygen reduction, Science 323 (2009) 760–764, https://doi.org/10.1126/science.1168049.

[9] J. Han, H. Bao, J.-Q. Wang, L. Zheng, S. Sun, Z.L. Wang, C. Sun, 3D N-doped ordered mesoporous carbon supported single-atom Fe-N-C catalysts with superior performance for oxygen reduction reaction and zinc-air battery, Appl. Catal. B: Environ. 280 (2021), 119411, https://doi.org/10.1016/j.apcatb.2020.119411.

[10] S. Chen, L. Ma, S. Wu, S. Wang, Z. Li, A.A. Emmanuel, M.R. Huqe, C. Zhi, J. A. Zapien, Uniform virus-like Co–N–Cs electrocatalyst derived from prussian blue analog for stretchable fiber-shaped zn–air batteries, Adv. Funct. Mater. 30 (2020) 1908945, https://doi.org/10.1002/adfm.201908945.

[11] J. Zheng, T. Kang, B. Liu, P. Wang, H. Li, M. Yang, N-doped carbon nanotubes encapsulated with FeNi nanoparticles derived from defect-rich, molecule-doped 3D g-C$_3$N$_4$ as an efficient bifunctional electrocatalyst for rechargeable zinc–air batteries, J. Mater. Chem. A 10 (2022) 9911–9921, https://doi.org/10.1039/D2TA00750A.

[12] K. Kim, K. Min, Y. Go, Y. Lee, S.E. Shim, D. Lim, S.-H. Baeck, FeCo alloy nanoparticles embedded in N-doped carbon supported on highly defective ketjenblack as effective bifunctional electrocatalysts for rechargeable Zn–air batteries, Appl. Catal. B: Environ. 315 (2022), 121501, https://doi.org/10.1016/j.apcatb.2022.121501.

[13] Y. Fu, H.-Y. Yu, C. Jiang, T.-H. Zhang, R. Zhan, X. Li, J.-F. Li, J.-H. Tian, R. Yang, NiCo alloy nanoparticles decorated on N-doped carbon nanofibers as highly active and durable oxygen electrocatalyst, Adv. Funct. Mater. 28 (2018) 1705094, https://doi.org/10.1002/adfm.201705094.

[14] Z.-D. Wang, S. Liang, C.-K. Bai, Z.-F. Guo, G.-L. Lu, H. Sun, Z.-N. Liu, H.-Y. Zang, Synergistically enhanced iron and zinc bimetallic sites as an advanced ORR electrocatalyst for flow liquid rechargeable Zn–air batteries, J. Mater. Chem. A 10 (2022) 3169–3177, https://doi.org/10.1039/D1TA09678H.

[15] K. Wang, X. Wang, Z. Li, B. Yang, M. Ling, X. Gao, J. Lu, Q. Shi, L. Lei, G. Wu, Y. Hou, Designing 3d dual transition metal electrocatalysts for oxygen evolution reaction in alkaline electrolyte: beyond oxides, Nano Energy 77 (2020), 105162, https://doi.org/10.1016/j.nanoen.2020.105162.

[16] X. Xie, W. Liu, T. Gong, Y. Wei, X. Lv, L. Fang, P. Sun, X. Sun, Iron-tin based nanoparticles anchored on N-doped carbon as high-efficiency oxygen electrocatalyst for rechargeable Zn-air batteries, Colloids Surf. A: Physicochem. Eng. Asp. 654 (2022), 130101, https://doi.org/10.1016/j.colsurfa.2022.130101.

[17] D. Xie, D. Yu, Y. Hao, S. Han, G. Li, X. Wu, F. Hu, L. Li, H.-Y. Chen, Y.-F. Liao, S. Peng, Dual-active sites engineering of N-doped hollow carbon nanocubes confining bimetal alloys as bifunctional oxygen electrocatalysts for flexible metal–air batteries, Small 17 (2021) 2007239, https://doi.org/10.1002/smll.202007239.

[18] Y. Cao, S. Huang, Z. Peng, F. Yao, X. Li, Y. Liu, H. Huang, M. Wu, Phase control of ultrafine FeSe nanocrystals in a N-doped carbon matrix for highly efficient and stable oxygen reduction reaction, J. Mater. Chem. A 9 (2021) 3464–3471, https://doi.org/10.1039/D0TA09544C.

[19] D.M. Morales, M.A. Kazakova, S. Dieckhöfer, A.G. Selyutin, G.V. Golubtsov, W. Schuhmann, J. Masa, Trimetallic Mn-Fe-Ni oxide nanoparticles supported on multi-walled carbon nanotubes as high-performance bifunctional ORR/OER electrocatalyst in alkaline media, Adv. Funct. Mater. 30 (2020) 1905992, https://doi.org/10.1002/adfm.201905992.

[20] X. Zhang, J. Luo, H.-F. Lin, P. Tang, J.R. Morante, J. Arbiol, K. Wan, B.-W. Mao, L.-M. Liu, J. Fransaer, Tailor-made metal-nitrogen-carbon bifunctional electrocatalysts for rechargeable Zn-air batteries via controllable MOF units, Energy Storage Mater. 17 (2019) 46–61, https://doi.org/10.1016/j.ensm.2018.11.034.

[21] X. Li, Y. Liu, H. Chen, M. Yang, D. Yang, H. Li, Z. Lin, Rechargeable Zn–Air batteries with outstanding cycling stability enabled by ultrafine FeNi nanoparticles-encapsulated N-doped carbon nanosheets as a bifunctional electrocatalyst, Nano Lett. 21 (2021) 3098–3105, https://doi.org/10.1021/acs.nanolett.1c00279.

[22] X. Zhu, D. Zhang, C.-J. Chen, Q. Zhang, R.-S. Liu, Z. Xia, L. Dai, R. Amal, X. Lu, Harnessing the interplay of Fe–Ni atom pairs embedded in nitrogen-doped carbon for bifunctional oxygen electrocatalysis, Nano Energy 71 (2020) 104597, https://doi.org/10.1016/j.nanoen.2020.104597.

[23] Z. Zhu, H. Yin, Y. Wang, C.-H. Chuang, L. Xing, M. Dong, Y.-R. Lu, G. Casillas-Garcia, Y. Zheng, S. Chen, Y. Dou, P. Liu, Q. Cheng, H. Zhao, Coexisting single-atomic Fe and Ni sites on hierarchically ordered porous carbon as a highly efficient ORR electrocatalyst, Adv. Mater. 32 (2020) 2004670, https://doi.org/10.1002/adma.202004670.

[24] L. Yang, X. Zeng, D. Wang, D. Cao, Biomass-derived FeNi alloy and nitrogen-codoped porous carbons as highly efficient oxygen reduction and evolution bifunctional electrocatalysts for rechargeable Zn-air battery, Energy Storage Mater. 12 (2018) 277–283, https://doi.org/10.1016/j.ensm.2018.02.011.

[25] L. Tong, Y.-C. Wang, M.-X. Chen, Z.-Q. Chen, Q.-Q. Yan, C.-L. Yang, Z.-Y. Zhou, S.-Q. Chu, X. Feng, H.-W. Liang, Hierarchically porous carbons as supports for fuel cell electrocatalysts with atomically dispersed Fe–Nx moieties, Chem. Sci. 10 (2019) 8236–8240, https://doi.org/10.1039/C9SC01154D.

[26] Z. Miao, X. Wang, M.-C. Tsai, Q. Jin, J. Liang, F. Ma, T. Wang, S. Zheng, B.-J. Hwang, Y. Huang, S. Guo, Q. Li, Atomically dispersed Fe-Nx/C electrocatalyst boosts oxygen catalysis via a new metal-organic polymer supramolecule strategy, Adv. Energy Mater. 8 (2018) 1801226, https://doi.org/10.1002/aenm.201801226.

[27] Q. Xu, Y. Tang, L. Zhai, Q. Chen, D. Jiang, Pyrolysis of covalent organic frameworks: a general strategy for template converting conventional skeletons into conducting microporous carbons for high-performance energy storage, Chem. Commun. 53 (2017) 11690–11693, https://doi.org/10.1039/C7CC07002K.

[28] J. Chmiola, G. Yushin, R. Dash, Y. Gogotsi, Effect of pore size and surface area of carbide derived carbons on specific capacitance, J. Power Sources 158 (2006) 765–772, https://doi.org/10.1016/j.jpowsour.2005.09.008.

[29] K. Yuan, D. Lützenkirchen-Hecht, L. Li, L. Shuai, Y. Li, R. Cao, M. Qiu, X. Zhuang, M.K.H. Leung, Y. Chen, U. Scherf, Boosting oxygen reduction of single iron active sites via geometric and electronic engineering: nitrogen and phosphorus dual coordination, J. Am. Chem. Soc. 142 (2020) 2404–2412, https://doi.org/10.1021/jacs.9b11852.

[30] D. Wang, H. Xu, P. Yang, L. Xiao, X. Du, X. Lu, R. Li, J. Zhang, M. An, A dual-template strategy to engineer hierarchically porous Fe–N–C electrocatalysts for the high-performance cathodes of Zn–air batteries, J. Mater. Chem. A 9 (2021) 9761–9770, https://doi.org/10.1039/D1TA00585E.

[31] L. Wu, B. Ni, R. Chen, P. Sun, T. Chen, A general approach for hierarchically porous metal/N/C nanosphere electrocatalysts: nano-confined pyrolysis of in situ-formed amorphous metal–ligand complexes, J. Mater. Chem. A 8 (2020) 21026–21035. ⟨https://doi.org/10.1039/D0TA07029G⟩.

[32] C. Zhu, Q. Shi, B.Z. Xu, S. Fu, G. Wan, C. Yang, S. Yao, J. Song, H. Zhou, D. Du, S. P. Beckman, D. Su, Y. Lin, Hierarchically porous M–N–C (M = Co and Fe) single-atom electrocatalysts with robust MNx active moieties enable enhanced ORR performance, Adv. Energy Mater. 8 (2018) 1801956, https://doi.org/10.1002/aenm.201801956.

[33] M. Wang, W. Yang, X. Li, Y. Xu, L. Zheng, C. Su, B. Liu, Atomically dispersed Fe–Heteroatom (N, S) bridge sites anchored on carbon nanosheets for promoting oxygen reduction reaction, ACS Energy Lett. 6 (2021) 379–386, https://doi.org/10.1021/acsenergylett.0c02484.

[34] D. Wu, J. Hu, C. Zhu, J. Zhang, H. Jing, C. Hao, Y. Shi, Salt melt synthesis of Chlorella-derived nitrogen-doped porous carbon with atomically dispersed CoN4 sites for efficient oxygen reduction reaction, J. Colloid Interf. Sci. 586 (2021) 498–504, https://doi.org/10.1016/j.jcis.2020.10.115.

[35] Y. Zhang, L.-B. Huang, W.-J. Jiang, X. Zhang, Y.-Y. Chen, Z. Wei, L.-J. Wan, J.-S. Hu, Sodium chloride-assisted green synthesis of a 3D Fe–N/C hybrid as a highly active electrocatalyst for the oxygen reduction reaction, J. Mater. Chem. A 4 (2016) 7781–7787. ⟨https://doi.org/10.1039/C6TA01655C⟩.

[36] R. Wu, X. Wan, J. Deng, X. Huang, S. Chen, W. Ding, L. Li, Q. Liao, Z. Wei, NaCl protected synthesis of 3D hierarchical metal-free porous nitrogen-doped carbon catalysts for the oxygen reduction reaction in acidic electrolyte, Chem. Commun. 55 (2019) 9023–9026, https://doi.org/10.1039/C9CC02986A.

[37] J. Hu, D. Wu, C. Zhu, C. Hao, C. Xin, J. Zhang, J. Guo, N. Li, G. Zhang, Y. Shi, Melt-salt-assisted direct transformation of solid oxide into atomically dispersed FeN4 sites on nitrogen-doped porous carbon, Nano Energy 72 (2020) 104670, https://doi.org/10.1016/j.nanoen.2020.104670.

[38] J. Li, S. Chen, W. Li, R. Wu, S. Ibraheem, J. Li, W. Ding, L. Li, Z. Wei, A eutectic salt-assisted semi-closed pyrolysis route to fabricate high-density active-site hierarchically porous Fe/N/C catalysts for the oxygen reduction reaction, J. Mater. Chem. A 6 (2018) 15504–15509. ⟨https://doi.org/10.1039/C8TA05419C⟩.

[39] Q. Li, P. Xu, W. Gao, S. Ma, G. Zhang, R. Cao, J. Cho, H.-L. Wang, G. Wu, Graphene/graphene-tube nanocomposites templated from cage-containing metal-organic frameworks for oxygen reduction in Li–O₂ batteries, Adv. Mater. 26 (2014) 1378–1386, https://doi.org/10.1002/adma.201304218.

[40] W. Xie, T. Tian, M. Yang, N. Li, L. Yu, Formation of hollow frameworks of dual-sided Fe/Fe₃C@N-doped carbon nanotubes as bifunctional oxygen electrocatalyst for Zn-air batteries, Appl. Catal. B: Environ. 317 (2022), 121760, https://doi.org/10.1016/j.apcatb.2022.121760.

[41] Q. Xiong, B. Liu, Y. Liu, P. Wang, H. Cheng, H. Li, Z. Lu, M. Yang, *In-situ* self-templating synthesis of 3D hierarchical porous carbons from oxygen-bridged porous organic polymers for high-performance supercapacitors, Nano Res. 15 (2022) 7759–7768. ⟨https://doi.org/10.1007/s12274-022-4452-x⟩.

[42] Z. Liu, Z. Zhao, Y. Wang, S. Dou, D. Yan, D. Liu, Z. Xia, S. Wang, In situ exfoliated, edge-rich, oxygen-functionalized graphene from carbon fibers for oxygen electrocatalysis, Adv. Mater. 29 (2017) 1606207, https://doi.org/10.1002/adma.201606207.

[43] X.F. Lu, S.L. Zhang, E. Shangguan, P. Zhang, S. Gao, X.W. Lou, Nitrogen-doped cobalt pyrite yolk–shell hollow spheres for long-life rechargeable zn–air batteries, Adv. Sci. 7 (2020) 2001178, https://doi.org/10.1002/advs.202001178.

[44] X. Lu, D. Wang, L. Ge, L. Xiao, H. Zhang, L. Liu, J. Zhang, M. An, P. Yang, Enriched graphitic N in nitrogen-doped graphene as a superior metal-free electrocatalyst for the oxygen reduction reaction, N. J. Chem. 42 (2018) 19665–19670, https://doi.org/10.1039/C8NJ04857F.

[45] C.-Y. Su, H. Cheng, W. Li, Z.-Q. Liu, N. Li, Z. Hou, F.-Q. Bai, H.-X. Zhang, T.-Y. Ma, Atomic modulation of FeCo–nitrogen–carbon bifunctional oxygen electrodes for rechargeable and flexible all-solid-state zinc–air battery, Adv. Energy Mater. 7 (2017) 1602420, https://doi.org/10.1002/aenm.201602420.

[46] D.M. Koshy, A.T. Landers, D.A. Cullen, A.V. Ievlev, H.M. Meyer Iii, C. Hahn, Z. Bao, T.F. Jaramillo, Direct characterization of atomically dispersed catalysts: nitrogen-coordinated Ni sites in carbon-based materials for CO₂ electroreduction, Adv. Energy Mater. 10 (2020) 2001836, https://doi.org/10.1002/aenm.202001836.

[47] M. Ma, A. Kumar, D. Wang, Y. Wang, Y. Jia, Y. Zhang, G. Zhang, Z. Yan, X. Sun, Boosting the bifunctional oxygen electrocatalytic performance of atomically dispersed Fe site via atomic Ni neighboring, Appl. Catal. B: Environ. 274 (2020), 119091. ⟨https://doi.org/10.1016/j.apcatb.2020.119091⟩.

[48] N. Yu, W. Cao, M. Huttula, Y. Kayser, P. Hoenicke, B. Beckhoff, F. Lai, R. Dong, H. Sun, B. Geng, Fabrication of FeNi hydroxides double-shell nanotube arrays with enhanced performance for oxygen evolution reaction, Appl. Catal. B: Environ. 261 (2020), 118193, https://doi.org/10.1016/j.apcatb.2019.118193.

[49] S. Yun, Y. Zhang, L. Zhang, Z. Liu, Y. Deng, Ni and Fe nanoparticles, alloy and Ni/Fe-Nₓ coordination co-boost the catalytic activity of the carbon-based catalyst for triiodide reduction and hydrogen evolution reaction, J. Colloid Inter. Sci. 615 (2022) 501–516, https://doi.org/10.1016/j.jcis.2022.01.192.

[50] Z. Wang, J. Ang, B. Zhang, Y. Zhang, X.Y.D. Ma, T. Yan, J. Liu, B. Che, Y. Huang, X. Lu, FeCo/FeCoNi/N-doped carbon nanotubes grafted polyhedron-derived hybrid fibers as bifunctional oxygen electrocatalysts for durable rechargeable zinc–air battery, Appl. Catal. B: Environ. 254 (2019) 26–36, https://doi.org/10.1016/j.apcatb.2019.04.027.

[51] X. Hao, Z. Jiang, B. Zhang, X. Tian, C. Song, L. Wang, T. Maiyalagan, X. Hao, Z.-J. Jiang, N-doped carbon nanotubes derived from graphene oxide with embedment of FeCo nanoparticles as bifunctional air electrode for rechargeable liquid and flexible all-solid-state zinc–air batteries, Adv. Sci. 8 (2021) 2004572, https://doi.org/10.1002/advs.202004572.

[52] Y. Tan, Z. Zhang, Z. Lei, L. Yu, W. Wu, Z. Wang, N. Cheng, Electronic modulation optimizes OH* intermediate adsorption on Co-Nx-C sites via coupling CoNi alloy in hollow carbon nanopolyhedron toward efficient reversible oxygen electrocatalysis, Appl. Catal. B: Environ. 304 (2022), 121006, https://doi.org/10.1016/j.apcatb.2021.121006.

[53] P. Liu, D. Gao, W. Xiao, L. Ma, K. Sun, P. Xi, D. Xue, J. Wang, Self-powered water-splitting devices by core–shell NiFe@N-graphite-based zn–air batteries, Adv. Funct. Mater. 28 (2018) 1706928, https://doi.org/10.1002/adfm.201706928.

[54] D. Bin, B. Yang, C. Li, Y. Liu, X. Zhang, Y. Wang, Y. Xia, In situ growth of NiFe alloy nanoparticles embedded into N-doped bamboo-like carbon nanotubes as a bifunctional electrocatalyst for Zn–Air batteries, Acs Appl. Mater. Inter 10 (2018) 26178–26187, https://doi.org/10.1021/acsami.8b04940.

[55] M.A. Kazakova, D.M. Morales, C. Andronescu, K. Elumeeva, A.G. Selyutin, A. V. Ishchenko, G.V. Golubtsov, S. Dieckhöfer, W. Schuhmann, J. Masa, Fe/Co/Ni mixed oxide nanoparticles supported on oxidized multi-walled carbon nanotubes as electrocatalysts for the oxygen reduction and the oxygen evolution reactions in alkaline media, Catal. Today 357 (2020) 259–268, https://doi.org/10.1016/j.cattod.2019.02.047.

[56] X. Lu, X. Tan, Q. Zhang, R. Daiyan, J. Pan, R. Chen, H.A. Tahini, D.-W. Wang, S. C. Smith, R. Amal, Versatile electrocatalytic processes realized by Ni, Co and Fe alloyed core coordinated carbon shells, J. Mater. Chem. A 7 (2019) 12154–12165, https://doi.org/10.1039/C9TA01723B.

[57] Y. He, S. Liu, C. Priest, Q. Shi, G. Wu, Atomically dispersed metal–nitrogen–carbon catalysts for fuel cells: advances in catalyst design, electrode performance, and durability improvement, Chem. Soc. Rev. 49 (2020) 3484–3524, https://doi.org/10.1039/C9CS00903E.

[58] J. Chen, H. Li, C. Fan, Q. Meng, Y. Tang, X. Qiu, G. Fu, T. Ma, Dual single-atomic Ni-N4 and Fe-N4 sites constructing janus hollow graphene for selective oxygen electrocatalysis, Adv. Mater. 32 (2020) 2003134, https://doi.org/10.1002/adma.202003134.

[59] J. Li, H. Zhang, W. Samarakoon, W. Shan, D.A. Cullen, S. Karakalos, M. Chen, D. Gu, K.L. More, G. Wang, Z. Feng, Z. Wang, G. Wu, Thermally driven structure and performance evolution of atomically dispersed FeN4 sites for oxygen reduction, Angew. Chem. Int. Ed. 58 (2019) 18971–18980, https://doi.org/10.1002/anie.201909312.

[60] M. Xiao, Z. Xing, Z. Jin, C. Liu, J. Ge, J. Zhu, Y. Wang, X. Zhao, Z. Chen, Preferentially Engineering FeN4 edge sites onto graphitic nanosheets for highly active and durable oxygen electrocatalysis in rechargeable zn–air batteries, Adv. Mater. 32 (2020) 2004900, https://doi.org/10.1002/adma.202004900.

[61] J.-F. Chen, Y. Mao, H.-F. Wang, P. Hu, Theoretical study of heteroatom doping in tuning the catalytic activity of graphene for triiodide reduction, ACS Catal. 6 (2016) 6804–6813, https://doi.org/10.1021/acscatal.6b01242.

[62] S. Wang, H. Wang, C. Huang, P. Ye, X. Luo, J. Ning, Y. Zhong, Y. Hu, Trifunctional electrocatalyst of N-doped graphitic carbon nanosheets encapsulated with CoFe alloy nanocrystals: The key roles of bimetal components and high-content graphitic-N, Appl. Catal. B: Environ. 298 (2021) 120512, https://doi.org/10.1016/j.apcatb.2021.120512.

[63] N. Xu, Y. Zhang, T. Zhang, Y. Liu, J. Qiao, Efficient quantum dots anchored nanocomposite for highly active ORR/OER electrocatalyst of advanced metal-air batteries, Nano Energy 57 (2019) 176–185, https://doi.org/10.1016/j.nanoen.2018.12.017.

[64] J.K. Nørskov, J. Rossmeisl, A. Logadottir, L. Lindqvist, J.R. Kitchin, T. Bligaard, H. Jónsson, Origin of the overpotential for oxygen reduction at a fuel-cell cathode, J. Phys. Chem. B 108 (2004) 17886–17892, https://doi.org/10.1021/jp047349j.

[65] I.C. Man, H.-Y. Su, F. Calle-Vallejo, H.A. Hansen, J.I. Martínez, N.G. Inoglu, J. Kitchin, T.F. Jaramillo, J.K. Nørskov, J. Rossmeisl, Universality in oxygen evolution electrocatalysis on oxide surfaces, ChemCatChem 3 (2011) 1159–1165, https://doi.org/10.1002/cctc.201000397.